Dynamics of a gas bubble in a straining flow: Deformation, oscillations, self-propulsion

Javier Sierra-Ausin, Paul Bonnefis, Antonia Tirri, David Fabre, Jacques Magnaudet

Dynamics of a gas bubble in a straining flow: deformation, oscillations, self-propulsion

Javier Sierra-Ausin,* Paul Bonnefis, Antonia Tirri,† David Fabre, and Jacques Magnaudet
Institut de Mécanique des Fluides de Toulouse (IMFT),
Université de Toulouse, CNRS, Toulouse, France.
(Dated: November 17, 2022)

We revisit from a dynamical point of view the classical problem of the deformation of a gas bubble suspended in an axisymmetric uniaxial straining flow. Thanks to a recently developed Linearized Arbitrary Lagrangian-Eulerian approach, we compute the steady equilibrium states and associated bubble shapes. Considering perturbations that respect the symmetries of the imposed carrying flow, we show that the bifurcation diagram is made of a stable and an unstable branch of steady states separated by a saddle-node bifurcation, the location of which is tracked throughout the parameter space. We characterize the most relevant global mode along each branch, namely an oscillatory mode that becomes neutrally stable in the inviscid limit along the stable branch, and an unstable non-oscillating mode eventually leading to the breakup of the bubble along the unstable branch. Next, considering perturbations that break the symmetries of the carrying flow, we identify two additional unstable non-oscillating modes associated with the possible drift of the bubble centroid away from the stagnation point of the undisturbed flow. One of them corresponds merely to a translation of the bubble along the elongational direction of the flow. The other is counterintuitive, as it corresponds to a drift of the bubble in the symmetry plane of the undisturbed flow, where this flow is compressional. We confirm the existence and characteristics of this mode by computing analytically the corresponding leading-order disturbance in the inviscid limit, and show that the observed dynamics are made possible by a specific self-propulsion mechanism that we explain qualitatively.

I. INTRODUCTION

The dynamics of a gas bubble (more generally a drop) freely suspended in a viscous fluid undergoing a uniaxial straining flow has received considerable attention since the pioneering work of Taylor [1]. When the fluid inertia cannot be neglected, the bubble shape results from the competion of pressure and viscous stresses that act to increase the interface deformation and the capillary stress that resists it. Under certain conditions, capillary effects are insufficient to keep the deformation finite, leading eventually to the breakup of the bubble. This physical configuration is commonly described in terms of the Weber (We) and Reynolds (Re) numbers which characterize the relative importance of inertial forces with respect to capillary and viscous forces, respectively. At low-but-finite Reynolds number, Acrivos & Lo [2] showed that no steady bubble shape exists beyond a critical Weber number, We_c, increasing as $\mathrm{Re}^{3/4}$. The same qualitative conclusion was reached in the inviscid limit by Miksis [3] who determined the corresponding $\mathcal{O}(1)$-value of We_c. Subsequently, Ryskin & Leal [4] computed the steady bubble shape over a wide range of We and Re by solving the full stationary Navier-Stokes equations on a boundary fitted grid. They found that We_c increases monotonically with Re and recovered with a good accuracy the predictions of [2] and [3] in the respective limits. These findings were confirmed by Kang & Leal [5] who considered the time-dependent bubble evolution, starting from some arbitrary initial shape. Among other things, they showed that the critical Weber number is highly sensitive to this initial condition, observing that it decreases as the initial elongation of the bubble is increased beyond that of the steady solution. They also considered the case of oscillating bubbles in the inviscid limit and showed that their oscillation frequency decreases as We increases and vanishes for $\mathrm{We} = \mathrm{We}_c$.

In this study, we revisit this rich phenomenology with the help of a global linear stability approach. Obviously, the chief technical difficulty in this free-boundary problem stands in the fact that the geometry of the flow domain is a priori unknown.This is why up to now it has been tackled numerically either with boundary integral methods in the creeping-flow limit ($\mathrm{Re} = 0$) [6, 7] or in the potential flow limit [8, 9], or with Navier-Stokes solvers making use of time-evolving boundary fitted grids [4, 5]. Here, we overcome this difficulty by making use of the recently developed Linearized Arbitrary Lagrangian-Eulerian approach [10], which allows the governing equations and boundary conditions of the problem to be expanded rigorously on an appropriate reference domain. We specify the problem in Sec. II and provide an overview of the Linearized Arbitrary Lagrangian-Eulerian methodology in appendix A. In Sec. III we take advantage of this approach to determine the complete bifurcation diagram of the system by considering perturbations

* javier.sierra@imft.fr; also at Department of Industrial Engineering (DIIN), University of Salerno UNISA, Fisciano, 84084, Italy
† Also at Department of Mechanics, Mathematics and Management, Polytechnic University of Bari, Bari, 70125, Italy

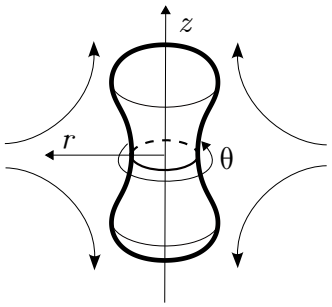

FIG. 1: Sketch of the physical configuration with the symmetry axis $r = 0$ and the symmetry plane $z = 0$ of the undisturbed straining flow, and the corresponding (r, θ, z) coordinate system.

respecting the symmetries of the imposed straining flow. This diagram is found to comprise a stable and an unstable branch connected through a saddle-node bifurcation. The stable branch corresponds to the previously computed steady states. The unstable branch, which was only reported before under creeping-flow conditions [7], is shown to be associated with the breakup of the bubble under subcritical conditions. In Sec. IV, we characterize the dominant linearly unstable or marginally stable mode of the system along each branch. By letting the bubble centroid move freely, we also identify two unstable modes that break the symmetries of the imposed straining flow and, to the best of our knowledge, were not described up to now. We observe that in one of them the bubble drifts away from the symmetry axis of the straining flow. We show that this surprising dynamics are associated with an original self-propulsion mechanism.

II. STATEMENT OF THE PROBLEM

We consider a gas bubble with negligible viscosity and constant volume $\mathcal{V}_b$ immersed in a Newtonian fluid, with dynamic viscosity μ and density ρ. The surface tension γ acting at the interface is assumed constant and the flow is considered incompressible. The fluid is subject to a uniaxial straining flow which, in the $(\mathbf{e}_r, \mathbf{e}_\theta, \mathbf{e}_z)$ basis sketched in Fig. 1, induces the velocity field $\mathbf{U}_\infty = -\frac{S}{2} r\mathbf{e}_r + Sz\mathbf{e}_z$, where S denotes the uniform strain rate. The bubble centroid stands initially at the origin $r = z = 0$ which is also the hyperbolic point of the straining flow. The stationary configuration (but not necessarily the eigenmodes to be considered later) is assumed to stay axisymmetric about the z-axis ($r = 0$) and also exhibits a mirror symmetry with respect to the midplane $z = 0$ (see fig. 1). Defining the equilibrium diameter d of the bubble such that $\mathcal{V}_b = \frac{\pi}{6} d^3$, we characterize the bubble deformation in the parameter space (Oh,We). The Ohnesorge number, $\mathrm{Oh} = \frac{\mu}{\sqrt{\rho\gamma d}}$, is defined as the ratio of the viscous force $\mu U_c d$ based on the capillary velocity scale $U_c = (\gamma/(\rho d))^{1/2}$ and the capillary force γd. Similarly, the Weber number, $\mathrm{We} = \frac{\rho S^2 d^3}{4\gamma}$, is defined as the ratio of the inertial force $\rho U_o^2 d^2$ based on the outer velocity scale $U_o = Sd/2$ and the capillary force. A Reynolds number may also be built by combining these two parameters in the form $\mathrm{Re} = \frac{\sqrt{\mathrm{We}}}{\mathrm{Oh}} = \frac{\rho U_o d}{\mu}$. The bubble elongation may be characterized through the aspect ratio $\chi = \frac{d_z}{d_r}$, with d_z and d_r the major and minor axis lengths, respectively.

Let $\Omega(t)$ and $\Gamma_b(t)$ denote the time-dependent fluid domain and bubble-fluid interface, respectively. The problem is governed by the set of equations

$$\partial_{t\Omega}\mathbf{u} + \mathbf{u}\cdot\nabla_\Omega\mathbf{u} = \rho^{-1}\nabla_\Omega\cdot\boldsymbol{\Sigma}_\Omega \quad \text{in } \Omega(t)\,, \tag{1}$$

$$\nabla_\Omega\cdot\mathbf{u} = 0 \quad \text{in } \Omega(t)\,, \tag{2}$$

$$\partial_{t\Omega}\eta = \mathbf{u}\cdot\mathbf{n} \quad \text{on } \Gamma_b(t)\,, \tag{3}$$

$$\boldsymbol{\Sigma}_\Omega\cdot\mathbf{n} = (-p_b + \gamma\kappa)\mathbf{n} \quad \text{on } \Gamma_b(t)\,, \tag{4}$$

supplemented with appropriate boundary conditions at $r = 0$, $z = 0$ and in the far field. In (1)-(4), the subscript $_\Omega$ is used to stress the fact that the time and space derivatives are to be evaluated in the time-dependent domain $\Omega(t)$. The no-penetration condition (3) implies that, at any location $\mathbf{x}$ on the interface, the time derivative of the interface position $\eta(\mathbf{x}, t)$ must coincide with the normal component $\mathbf{u}\cdot\mathbf{n}$ of the local fluid velocity $\mathbf{u}(\mathbf{x}, t)$, $\mathbf{n}(\mathbf{x}, t)$ denoting the local unit normal directed into the fluid. The stress tensor in the fluid is $\boldsymbol{\Sigma}_\Omega(\mathbf{u}, p) = -p\mathbf{I} + 2\mu\mathbf{D}_\Omega(\mathbf{u})$, with p, $\mathbf{I}$ and $\mathbf{D}_\Omega(\mathbf{u})$ the pressure, the unit tensor and the strain-rate tensor, respectively. The normal projection of (4) expresses the fact that the normal stress $\mathbf{n}\cdot\boldsymbol{\Sigma}_\Omega\cdot\mathbf{n}$ balances the difference between the uniform pressure $p_b(t)$ inside the bubble

and the local capillary pressure $\gamma\kappa\mathbf{n}$, with $\kappa(\mathbf{x},t) = \nabla\cdot\mathbf{n}(\mathbf{x},t)$ the local mean curvature of the interface. Last, the tangential projection of (4) yields the shear-free condition $\mathbf{n}\times(\mathbf{\Sigma}_\Omega\cdot\mathbf{n}) = \mathbf{0}$ which holds if the interface is free of any contamination.

Determining the steady solutions of (1)-(4) and performing subsequently a rigorous global linear stability analysis of the system is made difficult by the deformable nature of the fluid domain. Developing robust and efficient computational strategies to achieve this goal is currently an active research area in the field of fluid-structure interactions; e.g. [11, 12] and references therein. Here we adopt a Linearized Arbitrary Lagrangian-Eulerian approach, hereinafter referred to as L-ALE, which is a hybrid formulation combining the Eulerian and Lagrangian descriptions of the fluid motion. This approach, initially developed by one of us [10], is well adapted to the treatment of problems involving deformable fluid interfaces subjected to capillary forces. An overview of the L-ALE methodology and of its numerical implementation is given in appendix A.

An important strength of this approach is that steady-state solutions are computed using the steady form of the governing equations, i.e. the time derivatives in (1) and (3) are dropped. Making use of a Newton algorithm combined with a suitable continuation method (see appendix A), this allows the determination of both stable and unstable steady states, which would not be possible with a time-marching approach. Once a steady state is reached, its linear stability is assessed by examining the evolution of disturbances with a prescribed eigenmode form. In the present problem, the base configuration exhibits an axial symmetry about the z-axis. It is thus relevant to consider disturbances of velocity, pressure and position in the form $\Psi(r,z)e^{im\theta-i\omega t}$, with θ the polar angle in the cylindrical coordinate system sketched in Fig. 1 and m the corresponding wavenumber. Unstable eigenmodes satisfying $\mathcal{I}m(\omega) > 0$ can be classified as stationary (s) if $\mathcal{R}e(\omega) = 0$ or oscillating (o) if $\mathcal{R}e(\omega) \neq 0$. They can also be classified as symmetric (S) or antisymmetric (A) with respect to the plane $z = 0$. In what follows, we classify the modes using a nomenclature that summarizes their three characteristic properties, starting with their polar wavenumber m. For instance a '0 - S (s)' mode is axisymmetric ($m = 0$), symmetric with respect to the plane $z = 0$, and stationary.

III. BIFURCATION DIAGRAM

Figure 2(a) displays the bifurcation diagram obtained by setting the Ohnesorge number to the constant value $\mathrm{Oh} = 10^{-2}$. This diagram reveals the existence of two branches below a critical Weber number $\mathrm{We}_c \approx 2.27$ beyond which no stationary solution exists. Previous studies, for instance [5], showed that the bubble extends indefinitely when $\mathrm{We} > \mathrm{We}_c$ and eventually breaks up. We tracked the two branches found for $\mathrm{We} \leq \mathrm{We}_c$ using the pseudo-arc-length continuation method described in appendix A. Bubbles standing along the lower branch exhibit a convex shape while those along the upper branch are characterized by the presence of a concave neck in the symmetry plane. For a given $\mathrm{We} < \mathrm{We}_c$, solutions found along the lower branch (corresponding to the bubble with the smaller aspect ratio) are linearly stable in the sense that, following the nomenclature introduced above, all eigenmodes belonging to the 0 - S subspace are damped. In contrast, the solutions found along the upper branch are unstable due to the existence of an amplified eigenmode of the 0 - S (s) type. In the creeping-flow limit, Gallino *et al.* [7] identified this branch as an edge state of the underlying dynamical system, a qualification that still holds in the presence of finite-Reynolds-number effects. More precisely, if the initial conditions are located in the basin of attraction of this branch, the system first converges toward the corresponding steady state, before the solution becomes unstable at some point and the bubble eventually breaks up. The route to breakup then takes the form of a specific unstable deformation mode, hereinafter referred to as Mode 0-S (s), shown with thin red contours in fig. 2(a). Compared to the corresponding equilibrium shape, this mode is characterized by an increase in the bubble elongation and a reduction in the diameter of the neck. The parametric dependence of the critical Weber number with respect to the Reynolds number is reported in Fig. 2(b). Present results are found to agree well with those of [4] (solid black line). In particular, the $\mathrm{Re}^{3/4}$-dependence predicted in [2] (after it was reinterpreted in [4]) in the low-Re limit, and the asymptotic value $\mathrm{We}_c^\infty \approx 2.77$ determined in [3] in the inviscid limit are recovered. It may be observed that the stationary bubble shape corresponding to critical conditions is convex for intermediate and large Ohnesorge numbers, $\mathrm{Oh} \gtrsim \mathcal{O}(10^{-2})$ say, but becomes slightly concave in the neighborhood of the symmetry plane at lower Oh.

IV. LINEAR STABILITY

A. Symmetry-preserving unstable or least stable modes

In experiments, the bubble centroid is usually constrained to stay fixed at the stagnation point of the undisturbed flow using computer-controlled devices [13, 14]. Under such circumstances, the oscillations (for stable cases) or the

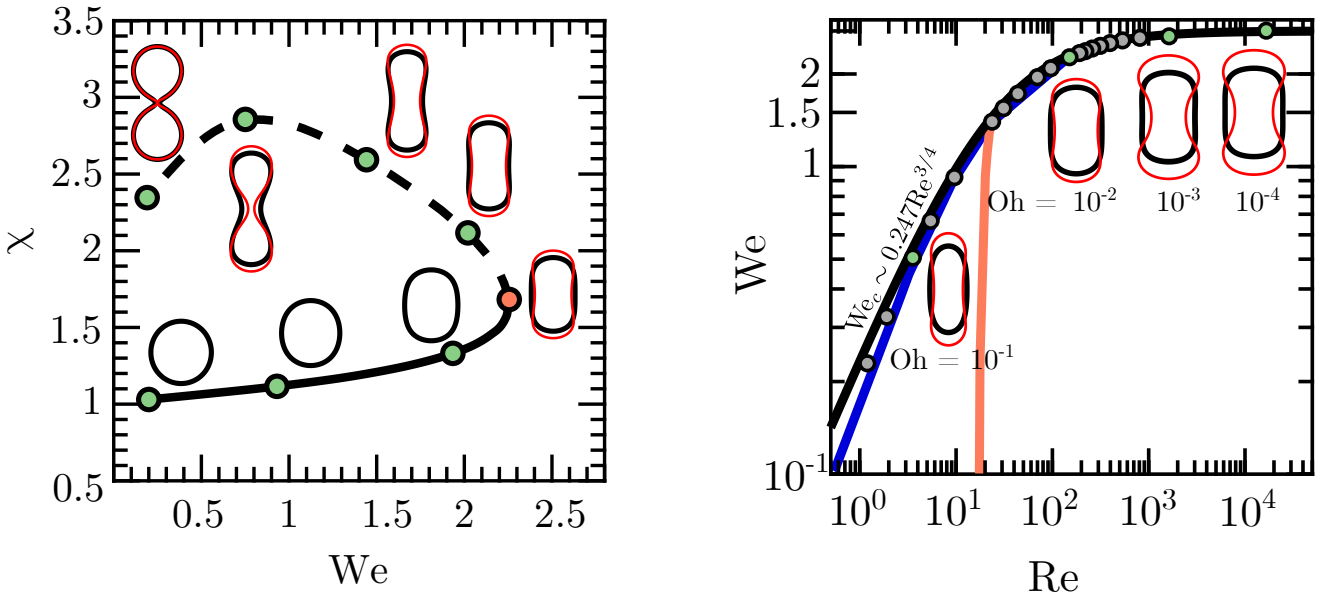

FIG. 2: Bifurcation diagram. (a): variation of the bubble elongation with the Weber number for a fixed value of the Ohnesorge number, here $\mathrm{Oh} = 10^{-2}$; (b) variation of the critical Weber number with the Reynolds number. Bullets: present results obtained with the L-ALE approach (the red bullet in (a) pinpoints the critical Weber number where the saddle-node bifurcation takes place); solid black line in ($a-b$): empirical correlation proposed in [4]; dashed line in (a): unstable branch determined with the continuation method. In (b), the blue line is the maximum Weber number $\mathrm{We} = \mathrm{We}_c^*(\mathrm{Re})$ beyond which Mode 0-S (o) stops oscillating; the red line indicates the minimum Reynolds number beyond which Mode 1-S (s) (see Sec. IV B) is unstable. In both panels, bubble shapes are shown for selected values of the parameters corresponding to the green bullets; the black and red contours correspond to the steady state and the unstable Mode 0-S (s), respectively.

deformations leading to breakup (for unstable cases) are expected to respect the polar and mirror symmetries of the base flow. This is why we first consider eigenmodes belonging to the subspace 0-S following the nomenclature introduced above. Two such modes emerge as the most unstable or least stable ones. One is the already mentioned unstable Mode 0-S (s), found along the upper branch of the bifurcation diagram. This mode is stationary, i.e. it is associated with a frequency such that $\mathcal{R}e(\omega) = 0$, and emerges from the saddle-node bifurcation at the critical Weber number We_c. In contrast, the second mode, hereinafter referred to as Mode 0-S (o), is oscillating and stable. Figure 3(a) shows how the frequency of this mode (black line) decreases as We increases and becomes eventually zero at a critical Weber number $\mathrm{We} = \mathrm{We}_c^*$. At this specific value, the complex eigenvalue associated with Mode 0-S (o) splits into two real eigenvalues. Both are negative, i.e. the corresponding two modes are damped, but they behave in opposite ways as $\mathrm{We} - \mathrm{We}_c^*$ increases within the interval $[\mathrm{We}_c^*, \mathrm{We}_c]$. The damping rate of the mode associated with the smallest eigenvalue (in absolute value) decreases continuously and vanishes eventually at $\mathrm{We} = \mathrm{We}_c$, leading to the amplification of Mode 0-S (s) beyond the saddle-node point (red line in Fig. 3(a)). In contrast, the damping rate of the original Mode 0-S (o) (green line in Fig. 3(a)) increases continuously from We_c^* to We_c, making this mode aperiodic throughout this interval. The spatial structure of modes 0-S (o) and 0-S (s) at a slightly subcritical Weber number ($\mathrm{We} = 2.5$) is illustrated in Fig. 3($b-c$). Mode 0-S (o) is associated with the complex eigenvalue $\omega = 1.3284 - 0.0044\mathrm{i}$ and therefore oscillates with a period $T = 2\pi/1.3284 \approx 4.73$. These oscillations result from the competition of inertial and capillary effects. They are characterized by a periodic sequence of compressional ($t = T/4$) and extensional ($t = 3T/4$) displacements of the bubble surface in the z-direction. Conversely, Mode 0-S (s) is unstable ($\omega = +0.2797\mathrm{i}$) and is characterized by a growing elongation of the bubble along its symmetry axis and a continuous shrinking wthin its equatorial plane.

Variations of the growth rate of Mode 0-S (s) with respect to $\mathrm{We}_c - \mathrm{We}$ are displayed in Fig. 4(a). The growth rate exhibits a marked increase with the distance to the threshold, scaling as $(\mathrm{We}_c - \mathrm{We})^\alpha$ with $\alpha = 1/4$ and $\alpha = 1/2$ in the high- and low-Reynolds-number limits, respectively. The $(\mathrm{We}_c - \mathrm{We})^{1/4}$-scaling is seen to hold up to $\mathrm{Oh} \approx 10^{-3}$, while the $(\mathrm{We}_c - \mathrm{We})^{1/2}$-scaling applies for $\mathrm{Oh} \gtrsim 10^{-1}$. Variations of the oscillation frequency (ω_r) of Mode 0-S

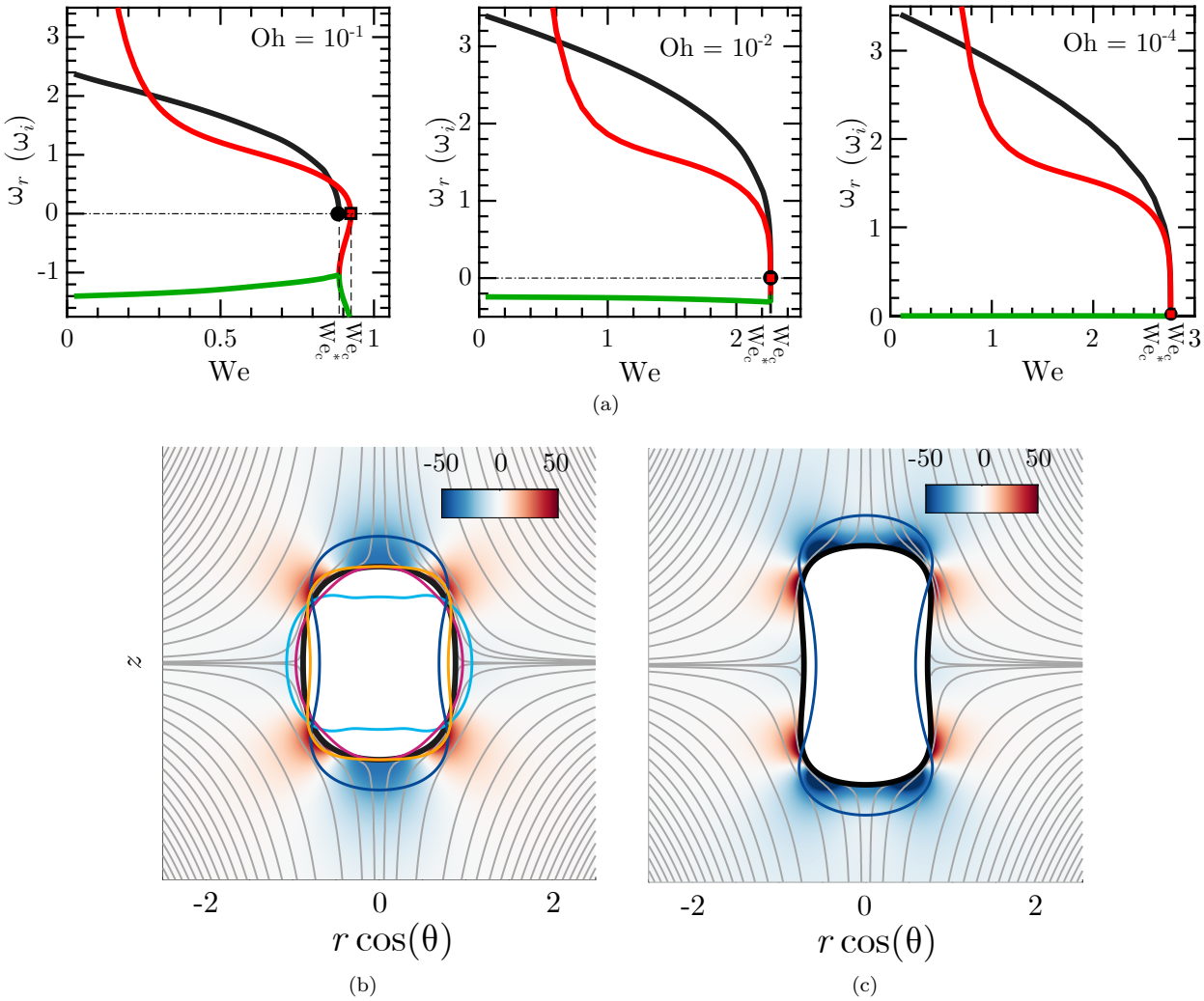

FIG. 3: (a): Variation of the frequency (black lines), growth rate of Mode 0-S (o) (green lines) and of Mode 0-S (s) (red lines) with respect to We, for three values of the Ohnesorge number. The black bullet and red square help to identify the critical Weber numbers We_c^* and We_c, respectively. (b): Pressure disturbance and bubble shape for Mode 0-S (o) (lower branch of the bifurcation diagram), for We = 2.5 and Oh = 1×10^{-4}. The black contour and grey lines represent the bubble shape and the streamlines in the base state, respectively. The colors show the imaginary part of the pressure disturbance at time $t = T/4$ and the contours display the bubble shape at $t = T/4$ (cyan), $t = T/2$ (orange), $t = 3T/4$ (dark blue), and $t = T$ (magenta), with T the period of oscillation. (c): Same for Mode 0-S (s) (upper branch of the bifurcation diagram), for the same (We, Oh) pair.

(o) with respect to $\mathrm{We}_c^* - \mathrm{We}$ are displayed in Fig. 5. The frequency is also found to grow as $(\mathrm{We}_c^* - \mathrm{We})^\alpha$ with $\alpha = 1/4$ and $\alpha = 1/2$ in the high- and low-Reynolds-number limits, respectively. The similarity of the above two scalings, albeit with the role of We_c played by We_c^* in the case of Mode 0-S (o), suggests a close connection between the dynamics of the two modes. As the respective positions of the black bullet and red square in Fig. 3(a) makes clear (see also the blue line in the range Re < 10 in Fig. 2(b)), We_c^* is slightly lower than We_c when viscous effects are large, and coincides with We_c when Oh $\to 0$. These findings are in line with those reported in [5]. That Mode 0-S (o) exhibits aperiodically damped oscillations within a finite interval $[\mathrm{We}_c^*(\mathrm{Oh}), \mathrm{We}_c(\mathrm{Oh})]$ in the presence of significant viscous effects was also pointed out in [15]. Indeed, assuming the steady bubble shape to be spherical and accounting for viscous effects in the dynamic boundary condition only through the influence of normal stresses (i.e. ignoring the shear-free condition), it was found in [15] that this aperiodically damped regime emerges for Oh $\gtrsim 0.12$. Based on an expansion around We $= 0$, it was predicted that ω_r scales as $(\mathrm{We}_{c0} - \mathrm{We})^{1/2}$, with $\mathrm{We}_{c0} \approx 3.23$. According to the inset in Fig. 5, this prediction holds for $\mathrm{We}_c^* - \mathrm{We} \gtrsim 0.3$ but fails to predict the rapid variations of the frequency near the critical Weber number.

The decay rate of Mode 0-S (o) is plotted in Fig. 4(b). This plot confirms the conclusion of Fig. 3(a), showing

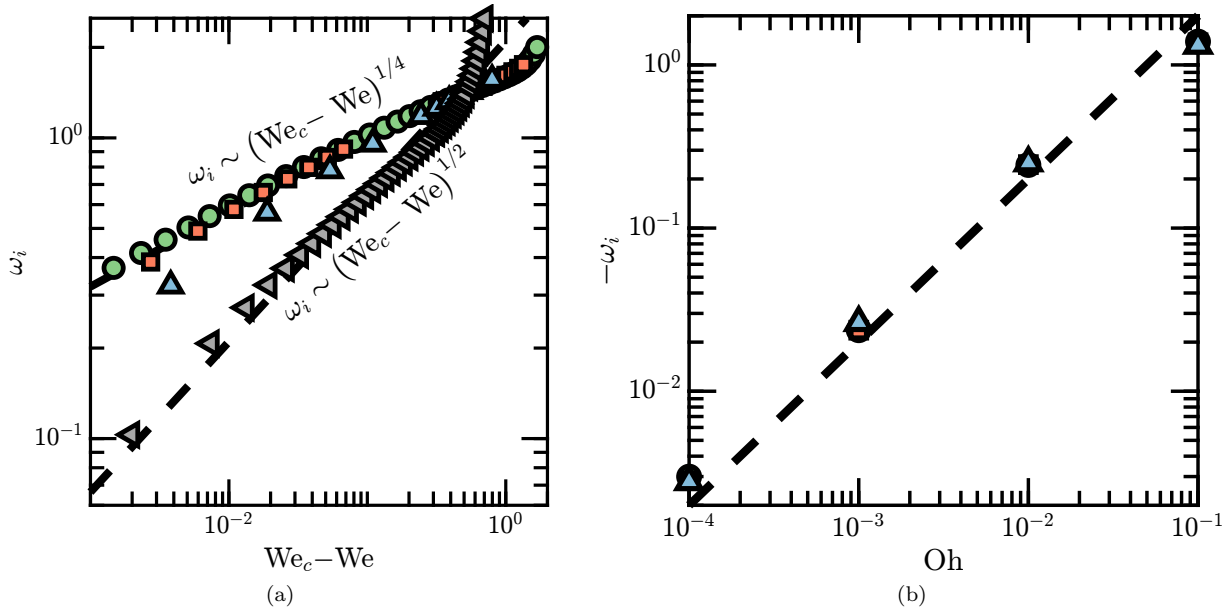

FIG. 4: Variations of the growth rate of modes 0-S (o) and 0-S (s). (a): with respect to $\mathrm{We}_c - \mathrm{We}$ for Mode 0-S (s) on the unstable branch; (b): with respect to Oh for Mode 0-S (o) on the stable branch. In (a), the green bullets, red squares, blue triangles and grey triangles refer to $\mathrm{Oh} = 10^{-4}, 10^{-3}, 10^{-2}$ and 10^{-1}, respectively; in (b), the green circles, red squares and blue triangles refer to $\mathrm{We} = 0.1, 0.2$ and 0.4, respectively. The dashed lines indicate the asymptotic scalings.

that this mode is stable throughout its domain of existence. Its decay rate increases linearly with Oh and is virtually independent of We. This mode becomes neutrally stable in the inviscid limit $\mathrm{Oh} \to 0$, and We_c^* then coincides with We_c as the right panel in Fig. 3(a) shows. This is no surprise since the problem becomes time-reversible in this limit and the bifurcation becomes a conservative saddle-node one, with two purely complex eigenvalues changing into two purely real ones. That Mode 0-S (o) is stable for finite Reynolds numbers indicates that inertial and capillary effects stay in balance in the corresponding dynamics, with viscous effects providing an additional stabilizing ingredient. This scenario works as long as the elongation of the bubble is small enough for the latter to remain in the basin of attraction of the stable steady state, i.e. close to the lower branch of the bifurcation diagram in Fig. 2(a). Conversely, if the bubble aspect ratio is large enough, breakup occurs through a Mode 0-S (s) deformation after the system has first approached the unstable (upper) branch of the bifurcation diagram and then moved away from it. In this case, the capillary force in the neck region close to the $z = 0$ symmetry plane is weaker than with a Mode 0-S (o) deformation having the same magnitude, owing to the larger concavity of the bubble surface (compare the blue contours in Figs. 3(b) and 3(c)). This makes the capillary force insufficient to balance the compressional force exerted by the base flow in that region. Beyond the linear stage considered here, this situation leads unavoidably to breakup through the classical end-pinching scenario [16, 17].

One can wonder how relevant the dynamics associated with the unstable branch of the bifurcation diagram are from an experimental point of view. In other words, how can this branch be reached in practice, and how Mode 0-S (s) can be triggered. Elements of answer stand in [16] which considered the transient response of a previously elongated drop once the extensional flow is stopped. It was observed that, provided the drop has reached a sufficient elongation prior to the stop, such that it has already taken a waisted shape, it eventually breaks up *via* an end-pinching instability [17] instead of relaxing towards its initial shape. These observations suggest that the unstable branch may be reached by first elongating the bubble for some time under suitable supercritical conditions, i.e. by imposing a Weber number $\mathrm{We}_1 > \mathrm{We}_c$, until the bubble attains the desired waisted shape. Then, after having identified the subcritical Weber number $\mathrm{We}_2 < \mathrm{We}_c$ at which the bubble achieves the same or a very similar stationary shape on the unstable branch, the imposed strain may be suitably reduced to decrease the Weber number $\mathrm{We}(t)$ down to the value We_2. Provided this transient is calibrated in such a way that the disturbance it generates remains small (which may represent a serious experimental challenge), the subsequent dynamics would correspond for some time to those of the linearly unstable Mode 0-S (s) described here.

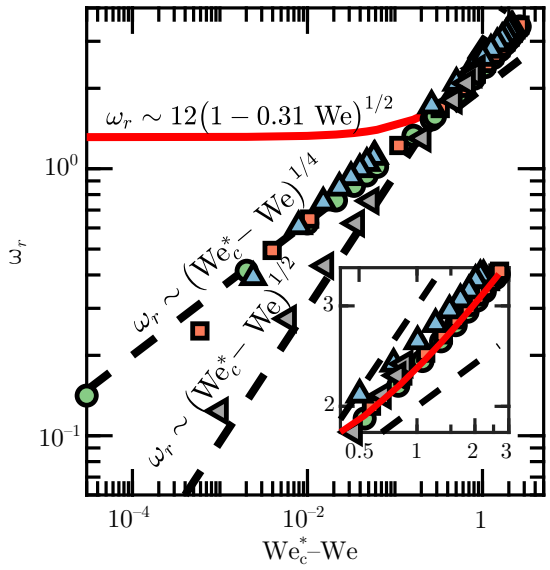

FIG. 5: Variation of the oscillation radian frequency ω_r of Mode 0-S (o) with respect to We. The black dashed lines correspond to the asymptotic scalings suggested by present result. The red line shows the low-We expansion of [15]. The green bullets, red squares, blue triangles and grey triangles refer to $\mathrm{Oh} = 10^{-4}, 10^{-3}, 10^{-2}$ and 10^{-1}, respectively. The inset provides a zoom on the range $0.5 \leq \mathrm{We}_c^* - \mathrm{We} \leq 3$.

B. Symmetry-breaking unstable modes

In cases where the bubble centroid is left free, one has to consider eigenmodes breaking either the axial symmetry about the $r = 0$ axis or the mirror symmetry about the $z = 0$ plane. Two new unstable modes are then detected. To the best of our knowledge, these modes have not been characterized so far. One of them, denoted as Mode 0-A (s), is unstable for every $(\mathrm{We}, \mathrm{Re})$. This mode is stationary but antisymmetric with respect to the plane $z = 0$. As Fig. 6(b) shows, this mode corresponds to a drift of the bubble centroid along the direction of elongation of the undisturbed flow. The existence of this unstable mode is the reason why in experiments a dynamic control such as that described in [14] has to be applied in order to prevent the bubble (or drop) from escaping along the extensional direction of the flow.

The second mode, which we refer to as Mode 1-S (s), is also stationary. It is symmetric with respect to the plane $z = 0$ and associated with the wavenumber $m = 1$ in the polar direction $\mathbf{e}_\theta$. As the red line in Fig. 2(b) indicates, this mode is unstable when the Reynolds number exceeds a value of the order of 20 which only weakly depends on the Weber number. Beyond this threshold the bubble is found to drift radially in the $z = 0$ plane; the direction of this drift is arbitrary since it is dictated by the definition of the angle θ. What is remarkable is that this drift is performed against the compressional component of the undisturbed flow. Since no external force is applied to the system, this unexpected motion may be thought of as an example of self-propulsion. The possibility for a deformable body immersed in a potential flow to self-propel was examined in several studies, especially [18–20]. It was concluded that a deformable body experiencing a net rate of deformation may self-propel provided its time-dependent shape presents some asymmetry. However, these references mostly considered oscillatory deformations of bodies moving in a fluid at rest. In contrast, the mode involved in the present case is stationary in the sense defined in Sec. II and the bubble moves in a straining flow. These two features make the present situation quite different from those envisaged in the aforementioned references.

The above predictions, especially those concerning Mode 1-S (s), need confirmation. For this purpose, following the approach of [15, 21], we considered the low-Oh (hence high-Re) regime and determined analytically to first order in We the evolution of a linear perturbation of the bubble shape, assuming that the disturbed flow is strictly irrotational. That is, assuming $\mathbf{u} = \nabla\phi$, we sought the harmonic function ϕ satisfying

$$\partial_t \eta = \nabla\phi \cdot \mathbf{n}\,, \quad \partial_t \phi + \frac{1}{2}(\nabla\phi \cdot \nabla\phi) + \rho^{-1} p_b = \rho^{-1}\gamma \nabla \cdot \mathbf{n} \quad \text{on } \Gamma_b\,. \tag{5}$$

For this, assuming that the Weber number is low enough for the undisturbed bubble to be close to a sphere, we

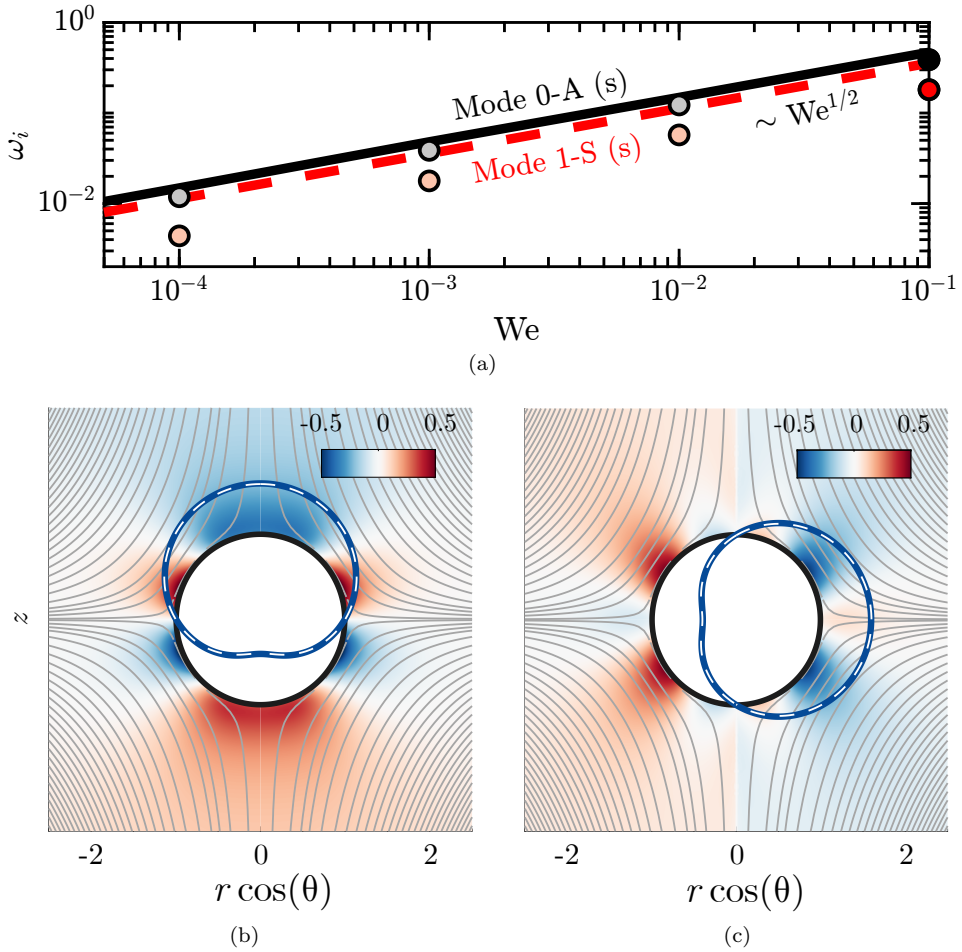

FIG. 6: Modes 0-A (s) and 1-S (s) in a high-Reynolds-number case. (a): variation of the growth rate of the two modes with respect to We, computed through the truncated potential flow solution of (7)-(8) (lines), and the L-ALE approach in a slightly viscous flow with Re=10^3 (bullets); black/grey: Mode 0-A (s), red/pink: Mode 1-S (s). (b): pressure disturbance (colours) and bubble shape (contours) for Mode 0-A (s) with We $= 10^{-1}$ and Re $= 10^3$, corresponding to the black bullet in (a). The almost superimposed blue and dashed white contours refer to the results provided by the L-ALE approach and the truncated potential flow solution, respectively. (c): same with Mode 1-S (s), corresponding to the red bullet in (a). In (b) – (c), the black contour represents the bubble shape in the base state and the grey lines show the corresponding streamlines.

expanded the velocity potential and the bubble shape in the form

$$\begin{array}{lll} \phi &= \frac{Sd^2}{4}(\phi_s + \varepsilon\phi_u^m)\,, & \eta = \frac{d}{2}(\eta_s + \varepsilon\eta_u^m)\,, \\ \phi_s &= P_2^0(\zeta)(\frac{1}{2}r_s^2 + \frac{1}{3}r_s^{-3})\,, & \eta_s = 1\,, \\ \phi_u^m &= \sum_{n=0}^{\infty}\chi_n^m(t)r_s^{-(n+1)}Y_n^m(\Theta,\varphi)\,, & \eta_u^m = \sum_{n=1}^{\infty}\delta_n^m(t)Y_n^m(\Theta,\varphi)\,, \end{array} \tag{6}$$

with $Y_n^m(\Theta,\varphi) = P_n^m(\zeta)e^{-\mathrm{i}m\varphi}$ the spherical harmonics, P_n^m the associated Legendre polynomial and $\zeta = \cos\Theta$. The corresponding spherical coordinate system is such that $\Theta = 0$ (π) on the positive (negative) half of the z-axis defined in Fig. 1, the meridional angle φ is equivalent to the angle θ defined in the same figure, and r_s is the radial position (normalized by $d/2$) measured from the centroid of the undisturbed bubble. Injecting the ansatz (6) in (5) and keeping only terms of $\mathcal{O}(\varepsilon)$ yields the eigenvalue problem

$$\begin{aligned} \dot{\chi}_n^m &= (n-1)(n+2)\delta_n^m \\ &+ \frac{5}{2}\left(\frac{1}{2}\mathrm{We}\right)^{\frac{1}{2}}\left\{\frac{(n-1-m)(n-m)(n-2)}{(2n-3)(2n-1)}\chi_{n-2}^m - \frac{n(n+1)-3m^2}{(2n-1)(2n+3)}\chi_n^m - \frac{(n+3)(n+1+m)(n+2+m)}{(2n+3)(2n+5)}\chi_{n+2}^m\right\}, \end{aligned} \tag{7}$$

$$\dot{\delta}_n^m = -(n+1)\chi_n^m \qquad (8)$$
$$+ \frac{5}{2}\big(\frac{1}{2}\mathrm{We}\big)^{\frac{1}{2}}\Big\{\frac{(n-1-m)(n-m)(n+1)}{(2n-3)(2n-1)}\delta_{n-2}^m + \frac{n(n+1)-3m^2}{(2n-1)(2n+3)}\delta_n^m - \frac{n(n+1+m)(n+2+m)}{(2n+3)(2n+5)}\delta_{n+2}^m\Big\},$$

with the dot denoting the time derivative. Solving the problem (7)-(8) for $m = 0$ and $m = 1$ up to $n = N_{max}$ (with N_{max} large enough that the eigenvalues no longer vary by further increasing the number of harmonics) reveals that modes 0-A (s) and 1-S (s) are also the most unstable ones in the potential flow limit. Their growth results from imbalances among the terms of the right-hand side of (7)-(8), which involve the velocity $\nabla\phi_s$ of the undisturbed straining flow. In (7), the imbalance is between the variations of the dynamic pressure, $-\nabla\phi_s \cdot \nabla\phi_u$, and those of the capillary pressure, $-\nabla\cdot(\nabla\eta_u)$. In (8), it is between the variations of the normal velocity at the interface induced by the velocity disturbance, $\mathbf{e}_{r_s}\cdot\nabla\phi_u$ (with $\mathbf{e}_{r_s}$ the unit radial vector), and those induced by the disturbance of the interface position, $-\nabla\phi_s\cdot\nabla\eta_u$. Figure 6($a$) shows how the growth rate of the two modes varies with We according to the above truncated potential model and to the L-ALE approach. Both solutions indicate that the growth rate increases as $\mathrm{We}^{1/2}$, as may be anticipated from the form of the right-hand sides in (7)-(8). The growth rate of Mode 1-S (s) is slightly smaller than that of Mode 0-A (s). Hence to observe the former in a laboratory experiment, it is necessary to prevent the bubble from moving along the z-axis. As the location of the bullets in the figure shows, the growth rates estimated with the L-ALE approach are lower than those resulting from the truncated potential flow model, especially in the case of Mode 1-S (s). This is due to the fact that finite-We effects affecting the steady state solution are not taken into account in the low-We potential flow expansion, nor are viscous effects arising in the boundary layer that surrounds the bubble. Although these effects are expected to be weak for $\mathrm{Re} = 10^3$, they are likely to be stabilizing, hence to reduce the growth rate. Despite these limitations, the truncated potential flow solution is found to provide a reliable estimate of the bubble deformation for modes 0-A (s) and 1-S (s) (dashed contour in Figs. 6(b) − (c)). At leading order, this deformation takes the form $\eta_u^0(\Theta,t) \propto \cos\Theta$ for Mode 0-A (s) and $\eta_u^1(\Theta,\phi,t) \propto \sin\Theta\cos\varphi$ for Mode 1-S (s). In summary, the above perturbative approach confirms that the presence of the unstable Mode 1-S (s) and its unexpected dynamics are not artifacts of the L-ALE approach. This mode is part of the intrinsic dynamical response of the system when the bubble centroid is not constrained to stay at the stagnation point of the uniaxial flow.

The bubble shapes and the pressure disturbance distribution displayed in Fig. 6(c) help to understand the physical mechanism that makes the self-propulsion associated with Mode 1-S (s) possible. Consider that the bubble is initially spherical and stands at the stagnation point. If a disturbance in the form of Mode 1-S (s) is applied, the geometric centroid of the bubble shifts to a radial position $r_0 \neq 0$. At this position, due to the radial pressure gradient $-\rho\frac{S^2}{4}r_0$ induced by the carrying flow, the disturbance past the bubble is no longer symmetric, even though the latter is still considered spherical. This pressure gradient is responsible for the left/right asymmetry in the pressure distribution of Fig. 6(c). That the pressure disturbance at the bubble surface reaches its extrema approximately midway between the z-axis and the symmetry plane $z = 0$ is a classical feature of a nearly-inviscid flow past a sphere translating in a straining flow (see e.g. [22]). These pressure extrema having opposite signs, they result in a net thrust (corresponding to an added-mass force) propelling the bubble in the direction opposite to the pressure gradient, i.e. from left to right in the figure. Moreover, the pressure on the outer side of the interface being equal to that within the bubble minus the capillary pressure, the asymmetric pressure distribution tends to make the bubble shape more asymmetric by decreasing (increasing) the mean curvature of the interface on the high- (low-) pressure side. Again, these deformations change the position of the bubble centroid, and they do it cooperatively with the above added-mass effect, as both mechanisms act to move the bubble to a position $r > r_0$ (i.e. to push it to the right in Fig. 6(c)). Since the inward velocity of the straining flow increases with r, so does the relative velocity between the carrying flow and the bubble centroid. This in turn enhances the pressure asymmetry at the bubble surface, which reinforces both the added-mass thrust and the asymmetric changes in the interface curvature, and so on. This qualitative scenario confirms that applying an asymmetric perturbation corresponding to the mode $m = 1$ to an initially spherical bubble resting at the stagnation point allows it to move radially thanks to what may be considered as a self-propulsion mechanism assisted by the straining flow. This mechanism grounds on the cooperative effect of capillary and inertial stresses, the latter resulting from the interaction of the carrying flow with the velocity disturbance. Of course this picture only holds as long as viscous effects are weak enough. Indeed, since the bubble leads the fluid, the drag resulting from the corresponding relative velocity resists the bubble drift (whereas the two cooperate in the case of Mode 0-(A) (s) in which the bubble lags the fluid). Therefore, it is only under conditions where this drag is small enough for the inertial forces involved in the above scenario to dominate that the bubble may drift. This is why Mode 1-S (s) only grows when the Reynolds number is large enough, i.e. $\mathrm{Re} \gtrsim 20$ according to the red line in Fig. 2(b). This is also why this intriguing behavior was not observed in the experiments of [13] in which the Reynolds number was kept very low (in the range $10^{-2} - 10^{-4}$) by using very viscous oils as suspending fluid.

V. SUMMARY

In this study, we employed the recently developed L-ALE approach to revisit the dynamics of a gas bubble immersed in a uniaxial straining flow. This approach proved to be able to accurately determine the equilibrium shapes of the bubble, as well as the maximum Weber number $\mathrm{We}_c(\mathrm{Oh})$ beyond which no equilibrium is possible. As already reported in the literature, the return to equilibrium of a slightly disturbed bubble under subcritical conditions takes place through damped oscillations, except within a small interval $[\mathrm{We}_c^*, \mathrm{We}_c]$ where an aperiodic damped regime takes place. We analyzed the eigenmode associated with these behaviors in detail. In particular, we characterized the scaling laws governing the variations of the corresponding eigenvalue with Oh and $\mathrm{We}_c^* - \mathrm{We}$. Thanks to a suitable continuation method, we also found a second branch of solutions linked to the branch of stable solutions through a saddle-node point. This branch was not identified up to now, except in the creeping-flow limit. Indeed, equilibrium shapes corresponding to this second branch are always unstable, which makes them unreachable with traditional time-marching approaches. The linear stability analysis revealed that the most amplified eigenmode on that branch is stationary and is characterized by the occurrence of a neck on the symmetry plane of the bubble. In the nonlinear stage, this would eventually lead to the breakup of the bubble through the end-pinching mechanism. We sketched how this unstable branch and the above stationary mode may be approached in a laboratory experiment. We also examined the case where the bubble centroid is not constrained to stay at the stagnation point of the undisturbed flow, a situation that was not considered in previous studies. In this case, two other unstable modes arise. The most amplified one corresponds to the drift of the bubble along the elongational axis of the undisturbed flow. Surprisingly, the slightly less amplified second mode leads to a drift of the bubble within the symmetry plane of the undisturbed flow, a region where this flow is directed toward the stagnation point. To check this unexpected prediction, we considered the low-We inviscid limit in which a truncated potential flow model can be established. We solved the corresponding eigenvalue problem and confirmed the predictions of the L-ALE approach in that limit. We also presented a qualitative scenario explaining why, after imposing an asymmetric initial perturbation to the bubble, the pressure and the interface curvature distributions develop growing asymmetric components that cooperate to make the bubble drift against the base flow possible when viscous effects are weak enough.

Appendix A: Overview of the L-ALE approach

Free-boundary problems involving a Newtonian fluid contained in a time-dependent fluid domain $\Omega(t)$ bounded by a fixed boundary Γ_s and a free boundary $\Gamma_b(t)$ subjected to capillary effects are governed by (1)-(4) supplemented with appropriate boundary conditions on Γ_s. In the L-ALE approach, we first consider a *reference* domain Ω_0, which is fixed and allows unknowns to be evaluated in an Eulerian manner, and the *physical* domain $\Omega(t)$, which depends upon time and where Lagrangian quantities are evaluated. Let $\mathbf{x}_0$ and $\mathbf{x}$ denote the local position (with respect to some fixed origin) of a given geometrical point in Ω_0 and Ω, respectively. Then, the two domains are connected through the diffeomorphism $\Phi : \Omega_0 \mapsto \Omega$, with $\Phi(\mathbf{x}_0, t) = \mathbf{x}$. In the L-ALE approach, this diffeomorphism is linearized in the form $\Phi(\mathbf{x}_0, t) = \mathbf{x}_0 + \boldsymbol{\xi}(\mathbf{x}_0)$, where $\boldsymbol{\xi}(\mathbf{x}_0)$ is a displacement field such that $||\boldsymbol{\xi}(\mathbf{x}_0)|| = ||\mathbf{x} - \mathbf{x}_0|| \sim O(\varepsilon_0||\mathbf{x}_0||)$ with $\varepsilon_0 \ll 1$. The field $\boldsymbol{\xi}(\mathbf{x}_0)$ propagates the Lagrangian displacement of the interface η into the fluid domain. This displacement field is arbitrary since it is not determined by the governing equations (1)-(4), i.e. it is not dictated by the actual motion of the fluid elements, except at the free boundary. It only needs to obey the no-penetration condition (3), plus some mild smoothness properties. Usually, the smoothness of $\boldsymbol{\xi}$ is ensured by assuming that its distribution within the fluid domain is governed by an elliptic equation, such as the Laplace equation or the Cauchy equation for an elastic material. An illustration of the L-ALE methodology is depicted in fig. 7(a). The sketch shows how the free boundary, labelled Γ_b in the physical domain Ω and $\Gamma_{b,0}$ in the reference domain Ω_0, transforms from one domain to the other. Although the geometric properties of this boundary, especially its unit normal $\mathbf{n}$ and tangent $\mathbf{t}$, may be evaluated in both domains, we always evaluate them in Ω_0, after which they may be mapped forward onto the physical domain via Φ if needed.

The L-ALE formalism leads to an approach in which the governing equations and the deformation of the physical domain are solved simultaneously and consistently, which ensures the stability of the algorithms involved. Such an approach, in which the unknown to be determined is the state vector $\mathbf{q} = [\mathbf{u}, p, p_b, \boldsymbol{\xi}, \eta]^{\mathrm{T}}$ ($^{\mathrm{T}}$ denoting the transpose), is sometimes referred to as 'monolithic'. To obtain the steady-state solution of (1)-(4), we solve the corresponding *steady* nonlinear problem using a Newton method, following the methodology introduced in [10].

That is, the steady-state solution, $\mathbf{q}_0 = [\mathbf{u}_0, p_0, p_{b,0}, \mathbf{0}, 0]^{\mathrm{T}}$, is determined iteratively by solving the system of

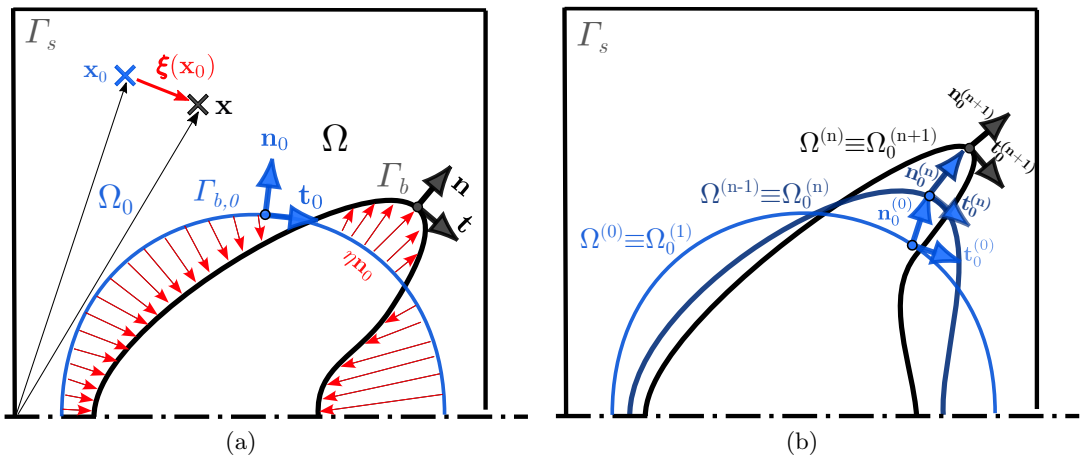

FIG. 7: Sketch of the geometrical transformations involved in the L-ALE approach. (a): general framework, showing in particular the current physical domain Ω and free boundary Γ_b (black), and the reference domain Ω_0 and free boundary $\Gamma_{b,0}$ (blue); (b): successive updates of the reference domain during the iterations of the Newton method.

equations governing the increment $\mathbf{q}' = [\mathbf{u}', p', p_b', \boldsymbol{\xi}, \eta]^{\mathrm{T}}$, namely

$$\begin{array}{rll}
\mathbf{L}_{NS}[\mathbf{q}'] & \equiv \mathbf{u}'\cdot\nabla_{\Omega_0}\mathbf{u}_0 + \mathbf{u}_0\cdot\nabla_{\Omega_0}\mathbf{u}' - \rho^{-1}\nabla_{\Omega_0}\cdot\boldsymbol{\Sigma}_{\Omega_0}(\mathbf{u}',p') + \mathbf{Q}_{\Omega_0}(\boldsymbol{\xi}) & = -\mathbf{u}_0\cdot\nabla_{\Omega_0}\mathbf{u}_0 + \rho^{-1}\nabla_{\Omega_0}\cdot\boldsymbol{\Sigma}_{\Omega_0} \quad \text{in } \Omega_0\,, \\
\mathbf{L}_{div}[\mathbf{q}'] & \equiv \nabla_{\Omega_0}\cdot\mathbf{u}' - \nabla_{\Omega_0}\mathbf{u}_0 \colon \nabla^{\mathrm{T}}_{\Omega_0}\boldsymbol{\xi} & = -\nabla_{\Omega_0}\cdot\mathbf{u}_0 \quad \text{in } \Omega_0\,, \\
\mathbf{L}_{kin}[\mathbf{q}'] & \equiv \mathbf{u}'\cdot\mathbf{n}_0 + \mathbf{u}_0\cdot\mathbf{n}' & = -\mathbf{u}_0\cdot\mathbf{n}_0 \quad \text{on } \Gamma_{b,0}\,, \\
\mathbf{L}_{dyn}[\mathbf{q}'] & \equiv (p_b' - p' - \gamma\kappa')\mathbf{n}_0 + 2\mu\mathbf{D}_{\Omega_0}(\mathbf{u}')\cdot\mathbf{n}_0 & = (p_0 - p_{b,0} + \gamma\kappa_0)\mathbf{n}_0 \quad \text{on } \Gamma_{b,0}\,, \\
 & \quad +(p_{b,0} - p_0 - \gamma\kappa_0)\mathbf{n}' + 2\mu\mathbf{D}_{\Omega_0}(\mathbf{u}_0)\cdot\mathbf{n}' & \quad -2\mu\mathbf{D}_{\Omega_0}(\mathbf{u}_0)\cdot\mathbf{n}_0 \\
\mathbf{L}_{com}[\mathbf{q}'] & \equiv \boldsymbol{\xi} - \eta\mathbf{n}_0 & = \mathbf{0} \quad \text{on } \Gamma_{b,0}\,, \\
\mathbf{L}_{E}[\boldsymbol{\xi}] & \equiv \nabla_{\Omega_0}\cdot\mathbf{E}(\boldsymbol{\xi}) & = \mathbf{0} \quad \text{in } \Omega_0\,,
\end{array} \tag{A1}$$

where the $_{\Omega_0}$ subscript indicates that the corresponding spatial derivative is evaluated in the reference domain Ω_0 bounded (partly) by the free boundary $\Gamma_{b,0}$. In (A1), the first four equations correspond to the linearized form of the governing equations (1)-(4). The deformation of the domain induces several extra terms in these linearized equations, especially an extra momentum source term $\mathbf{Q}_{\Omega_0}(\boldsymbol{\xi}) = -\mathbf{u}_0\cdot\nabla_{\Omega_0}\mathbf{u}_0\cdot\nabla_{\Omega_0}\boldsymbol{\xi} + \rho^{-1}(\nabla_{\Omega_0}\cdot\boldsymbol{\Sigma}_{\Omega_0})\cdot\nabla^{\mathrm{T}}_{\Omega_0}\boldsymbol{\xi} + \rho^{-1}\mu\nabla_{\Omega_0}\cdot\left\{\nabla_{\Omega_0}\mathbf{u}_0\cdot\nabla_{\Omega_0}\boldsymbol{\xi} + (\nabla_{\Omega_0}\mathbf{u}_0\cdot\nabla_{\Omega_0}\boldsymbol{\xi})^{\mathrm{T}}\right\}$ in the momentum equation. The last two equations determine the displacement field $\boldsymbol{\xi}$ throughout the domain. The elliptic operator $\mathbf{E}$ controls the spatial distribution of this arbitrary displacement within Ω_0, subject to the compatibility condition $\boldsymbol{\xi} = \eta'\mathbf{n}_0$ on $\Gamma_{b,0}$. Here, following [12], we assume that this distribution obeys a linear elastic response, i.e. we set $\mathbf{E}(\boldsymbol{\xi}) = 2\mu_e\mathbf{D}_{\Omega_0}(\boldsymbol{\xi}) + \lambda_e(\nabla_{\Omega_0}\cdot\boldsymbol{\xi})\mathbf{I}$. With this choice, the last equation in (A1) may be interpreted as the Cauchy equation of elasticity, the coefficients λ_e and μ_e being Lamé pseudo-coefficients which we both set to unity.

At each iteration n, the pseudo-steady state solution is updated in the form $\mathbf{q}_0^{(n)} = \mathbf{q}_0^{(n-1)} + \mathbf{q}' = [\mathbf{u}_0 + \mathbf{u}', p_0 + p', p_{b,0} + p_b', \boldsymbol{\xi}, \eta]^{\mathrm{T}}$. The reference domain Ω_0 is also updated, based on conditions $\mathbf{x}_{\Omega_0^{(n)}} = \mathbf{x}_{\Omega_0^{(n-1)}} + \boldsymbol{\xi}$ and $\mathbf{x}_{\Gamma_0^{(n)}} = \mathbf{x}_{\Gamma_0^{(n-1)}} + \eta$ linking the position of a given point standing in the fluid domain or on the free boundary in two successive reference configurations, as sketched in fig. 7(b). In other words, the steady-state solution is obtained by considering the governing equations (A1) on a succession of physical domains such that the n^{th} of them only differs slightly from the $(n-1)^{\text{th}}$ one, the latter being considered as the new reference domain during the n^{th}-iteration.

In cases where the free boundary is a closed surface (such as for a bubble), the enclosed volume must stay equal to its initial value, $\mathcal{V}_b$, provided effects of compressibility are negligible in the corresponding medium. This implies

$$\mathbf{L}_{vol}[\mathbf{q}'] \equiv \int_{\Gamma_{b,0}} \eta d\mathcal{S}_0 = \int_{\Omega_{b,0}} (1 + \nabla_{\Omega_0}\cdot\boldsymbol{\xi}) d\mathcal{V}_0 - \mathcal{V}_b \quad \text{on } \Gamma_{b,0}\,. \tag{A2}$$

The various matrices involved in the problem (A1)-(A2) are built and inverted within the finite-element software FreeFem++. The volume fields $(\mathbf{u}, p)$ are discretized following a Taylor–Hood scheme, i.e. the mixed finite-element Lagrange basis (P_2,P_1). The volume displacement field $\boldsymbol{\xi}$ is discretized within the P_2 finite-element space. The free-boundary displacement field η is discretized within the Galerkin-Fourier space. This displacement is orthogonally

projected onto the local Fourier basis ϕ_k in the form $\eta(s_0) = \sum_{k=0}^{N_b} \phi_k(s_0) X_\eta(k)$, with $X_\eta(k)$ the coefficients of η in that basis, N_b the number of Fourier elements and s_0 the arc length coordinate.

In the vicinity of a saddle-node bifurcation, the Jacobian matrix of (A1) is ill-conditioned. In particular it is singular at the bifurcation point. In such situations, instead of the usual continuation procedure performed on some control parameter, for instance We, we continue the solution on a suitable arc length with a pseudo-arc-length continuation method. This technique consists in replacing the Jacobian matrix with a bordered matrix, i.e. a matrix with an additional column and an additional row. The practical application of this technique, i.e. the definition of the arc length, depends on the parameters of the problem under consideration. In the context of this paper, we build the arc length on the pressure within the bubble, p_b, and the strain rate of the base flow, S, so that the infinitesimal arc length is $(ds)^2 = (dp_b)^2 + (dS)^2$. If (A1) (or (A1)-(A2)) is written symbolically in the form $\mathbf{L}|_{\mathbf{q}_0}[\mathbf{q}'] = -\mathbf{F}(\mathbf{q}_0)$, the bordered system then takes the form

$$\begin{pmatrix} \mathbf{L}|_{\mathbf{q}_0^{(n-1)}} & \mathbf{D}_{bc} \\ \frac{dp_b}{ds} & \frac{dS}{ds} \end{pmatrix} \begin{pmatrix} \mathbf{q}' \\ S' \end{pmatrix} = \begin{pmatrix} -\mathbf{F}(\mathbf{q}_0^{(n-1)}) - \mathbf{D}_{bc}(S_0^{(n-1)}) \\ -\frac{dp_b}{ds}(p_{b,0}^{(n-1)} - p_{b,0}^{(0)}) - \frac{dS}{ds}(S_0^{(n-1)} - S_0^{(0)}) + \Delta s \end{pmatrix}, \tag{A3}$$

where the state vector $\mathbf{q}'$ is augmented with the update of the strain rate, S', and Δs denotes the arc length step. The operator $\mathbf{D}_{bc}$, which takes the form of a column vector in the bordered matrix, serves to impose the boundary conditions on the velocity field and only depends on S. The derivative $\frac{dp_b}{ds}$ acts on the pressure within the bubble only, while $\frac{dS}{ds}$ only acts on the strain rate. These derivatives are determined at the initial step of the Newton method by inverting the matrix operator $\mathbf{L}|_{\mathbf{q}_0^{(0)}}$ and computing the derivative of $\mathbf{q}$ with respect to S as $\frac{d\mathbf{q}}{dS}|_{\mathbf{q}_0^{(0)}} = -\mathbf{L}^{-1}|_{\mathbf{q}_0^{(0)}} \cdot \frac{d\mathbf{F}}{dS}(\mathbf{q}_0^{(0)})$. Then, selecting the component $\frac{dp_b}{dS}|_{\mathbf{q}_0^{(0)}}$ in the vector field $\frac{d\mathbf{q}}{dS}|_{\mathbf{q}_0^{(0)}}$ and making use of the definition $(ds)^2 = (dp_b)^2 + (dS)^2$, the extra derivatives involved in (A3) are computed as $\frac{dp_b}{ds} = \frac{dp_b}{dS}|_{\mathbf{q}_0^{(0)}} \{(\frac{dp_b}{dS}|_{\mathbf{q}_0^{(0)}})^2 + 1\}^{-1/2}$ and $\frac{dS}{ds} = \{(\frac{dp_b}{dS}|_{\mathbf{q}_0^{(0)}})^2 + 1\}^{-1/2}$.

Once the steady state is reached, the linear stability of the corresponding solution is determined by examining the fate of disturbances with the eigenmode form $\mathbf{q}' = [\hat{\mathbf{u}}, \hat{p}, \hat{p}_b, \hat{\boldsymbol{\xi}}, \hat{\eta}]^{\mathrm{T}} e^{-i\omega t}$, the hatted complex amplitudes depending on $\mathbf{x}_0$. In cases where the base configuration is axisymmetric, as in the physical problem considered in this paper, we rather consider disturbances of the form $\mathbf{q}' = [\hat{\mathbf{u}}, \hat{p}, \hat{p}_b, \hat{\boldsymbol{\xi}}, \hat{\eta}]^{\mathrm{T}} e^{im\theta - i\omega t}$, with θ the polar angle of the (r, θ, z) cylindrical coordinate system and m the corresponding wavenumber, the hatted amplitudes depending now only on r and z. Such solutions are obtained by solving the eigenvalue problem

$$\begin{aligned} -\mathrm{i}\omega\big(\hat{\mathbf{u}} - \hat{\boldsymbol{\xi}} \cdot \nabla_{\Omega_0} \mathbf{u}_0\big) + \mathbf{L}_{NS}[\hat{\mathbf{q}}] &= \mathbf{0} \quad \text{in } \Omega_0\,, \\ \mathbf{L}_{div}[\hat{\mathbf{q}}] &= 0 \quad \text{in } \Omega_0\,, \\ -\mathrm{i}\omega\hat{\eta} + \mathbf{L}_{kin}[\hat{\mathbf{q}}] &= 0 \quad \text{on } \Gamma_{b,0}\,, \\ \mathbf{L}_{dyn}[\hat{\mathbf{q}}] &= \mathbf{0} \quad \text{on } \Gamma_{b,0}\,, \\ \mathbf{L}_{com}[\hat{\mathbf{q}}] &= \mathbf{0} \quad \text{on } \Gamma_{b,0}\,, \\ \mathbf{L}_{E}[\hat{\boldsymbol{\xi}}] &= \mathbf{0} \quad \text{in } \Omega_0\,, \end{aligned} \tag{A4}$$

supplemented with

$$\mathbf{L}_{vol}[\hat{\mathbf{q}}] = 0 \quad \text{on } \Gamma_{b,0} \tag{A5}$$

if the constraint (A2) holds for the steady-state and the perturbation. In (A4), the term $\mathrm{i}\omega\hat{\boldsymbol{\xi}} \cdot \nabla_{\Omega_0}\mathbf{u}_0$ arising in the linearized momentum equation is the acceleration of the moving domain, which must be subtracted to obtain the actual fluid acceleration in Ω_0. Here, the reference domain is that corresponding to the steady-state solution of (A1), i.e. $\Omega_0 \equiv \Omega_0^{(N)}$, with N the number of iterations carried out to reach the steady solution through the Newton method, as depicted in fig. 7(b). The eigenpairs of (A4)-(A5) are obtained using the SLEPc library.

[1] G. I. Taylor, The formation of emulsions in definable fields of flow, Proc. R. Soc. London Ser. A-Math. Phys. Eng. Sci. **146**, 501 (1934).

[2] A. Acrivos and T. S. Lo, Deformation and breakup of a single slender drop in an extensional flow, J. Fluid Mech. **86**, 641 (1978).

[3] M. J. Miksis, A bubble in an axially symmetric shear flow, Phys. Fluids **24**, 1229 (1981).

[4] G. Ryskin and L. G. Leal, Numerical solution of free-boundary problems in fluid mechanics. Part 3. Bubble deformation in an axisymmetric straining flow, J. Fluid Mech. **148**, 37 (1984).

[5] I. S. Kang and L. G. Leal, Numerical solution of axisymmetric, unsteady free-boundary problems at finite Reynolds number. I. Finite-difference scheme and its application to the deformation of a bubble in a uniaxial straining flow, Phys. Fluids **30**, 1929 (1987).

[6] G. K. Youngren and A. Acrivos, On the shape of a gas bubble in a viscous extensional flow, J. Fluid Mech. **76**, 433 (1976).

[7] G. Gallino, T. M. Schneider, and F. Gallaire, Edge states control droplet breakup in subcritical extensional flows, Phys. Rev. Fluids **3**, 073603 (2018).

[8] J. Rodriguez-Rodriguez, J. M. Gordillo, and C. Martinez-Bazan, Breakup time and morphology of drops and bubbles in a high-Reynolds-number flow, J. Fluid Mech. **548**, 69 (2006).

[9] J. C. Padrino and D. D. Joseph, Viscous irrotational analysis of the deformation and break-up time of a bubble or drop in uniaxial straining flow, J. Fluid Mech. **688**, 390 (2011).

[10] P. Bonnefis, *Etude des instabilités de sillage, de forme et de trajectoire de bulles par une approche de stabilité linéaire globale*, Ph.D. thesis, Inst. Nat. Polytech. Toulouse, Toulouse, France (available online at http://www.theses.fr/2019INPT0070) (2019).

[11] M. Heil, A. L. Hazel, and J. Boyle, Solvers for large-displacement fluid-structure interaction problems: segregated versus monolithic approaches, Comput. Mech. **43**, 91 (2008).

[12] J. L. Pfister, O. Marquet, and M. Carini, Linear stability analysis of strongly coupled fluid–structure problems with the Arbitrary Lagrangian–Eulerian method, Comput. Meth. Appl. Mech. Eng. **355**, 663 (2019).

[13] B. J. Bentley and L. G. Leal, An experimental investigation of drop deformation and breakup in steady, two-dimensional linear flows, J. Fluid Mech. **167**, 241 (1986).

[14] B. J. Bentley and L. G. Leal, A computer-controlled four-roll mill for investigations of particle and drop dynamics in two-dimensional linear shear flows, J. Fluid Mech. **167**, 219 (1986).

[15] I. S. Kang and L. G. Leal, Small-amplitude perturbations of shape for a nearly spherical bubble in an inviscid straining flow (steady shapes and oscillatory motion), J. Fluid Mech. **187**, 231 (1988).

[16] H. A. Stone, B. J. Bentley, and L. G. Leal, An experimental study of transient effects in the breakup of viscous drops, J. Fluid Mech. **173**, 131 (1986).

[17] H. A. Stone and L. G. Leal, Relaxation and breakup of an initially extended drop in an otherwise quiescent fluid, J. Fluid Mech. **198**, 399 (1989).

[18] P. G. Saffman, The self-propulsion of a deformable body in a perfect fluid, J. Fluid Mech. **28**, 385 (1967).

[19] T. B. Benjamin and A. T. Ellis, Self-propulsion of asymmetrically vibrating bubbles, J. Fluid Mech. **212**, 65 (1990).

[20] T. Miloh and A. Galper, Self-propulsion of general deformable shapes in a perfect fluid, Proc. R. Soc. London Ser. A-Math. Phys. Eng. Sci. **442**, 273 (1993).

[21] S. M. Yang, Z. C. Feng, and L. G. Leal, Nonlinear effects in the dynamics of shape and volume oscillations for a gas bubble in an external flow, J. Fluid Mech. **247**, 417 (1993).

[22] J. Magnaudet, M. Rivero, and J. Fabre, Accelerated flows past a rigid sphere or a spherical bubble. Part 1. Steady straining flow, J. Fluid Mech. **284**, 97 (1995).